

Quantum Critical Scaling of Fidelity Susceptibility

A. Fabricio Albuquerque,^{1,2} Fabien Alet,^{1,2} Clément Sire,^{1,2} and Sylvain Capponi^{1,2}

¹Laboratoire de Physique Théorique, Université de Toulouse, UPS (IRSAMC), F-31062 Toulouse, France

²CNRS, LPT (IRSAMC), F-31062 Toulouse, France

(Dated: May 30, 2022)

The behavior of the ground-state fidelity susceptibility in the vicinity of a quantum critical point is investigated. We derive scaling relations describing its singular behavior in the quantum critical regime. Unlike in previous studies, these relations are solely expressed in terms of conventional critical exponents. We also describe in detail a quantum Monte Carlo scheme that allows for the evaluation of the fidelity susceptibility for a large class of many-body systems and apply it in the study of the quantum phase transition for the transverse-field Ising model on the square lattice. Finite size analysis applied to the so obtained numerical results confirm the validity of our scaling relations. Furthermore, we analyze the properties of a closely related quantity, the ground-state energy's second derivative, that can be numerically evaluated in a particularly efficient way. The usefulness of both quantities as alternative indicators of quantum criticality is examined.

PACS numbers: 75.10.Jm, 64.70.Tg, 03.67.-a, 02.70.Ss

I. INTRODUCTION

The quantity known as *fidelity* naturally appears in the field of quantum information science as a way of determining the reliability of a given protocol for quantum information transfer: the similarity between input $|\Psi_{\text{in}}\rangle$ and output $|\Psi_{\text{out}}\rangle$ states can be quantified by simply computing the absolute value of the overlap between them, $F = |\langle\Psi_{\text{in}}|\Psi_{\text{out}}\rangle|$. Recently, after the pioneering work¹ of Zanardi and Paunković, and following the broader trend of cross-fertilization between the fields of quantum information science and condensed matter physics,² a number of studies have extended the scope of applicability of the concept of fidelity to the study of quantum critical phenomena (for a review, see Ref. 3).

The basic idea behind this so-called *fidelity approach* is simple. We consider a general many-body Hamiltonian

$$\mathcal{H}(g) = H_0 + gH_1, \quad (1)$$

with ground-state $|\Psi_0(g)\rangle$, $\mathcal{H}(g)|\Psi_0(g)\rangle = E_0(g)|\Psi_0(g)\rangle$. Since $|\Psi_0(g)\rangle$ undergoes major changes in the vicinity of a quantum critical point (QCP) g_c , we expect a sharp drop in the fidelity,

$$F(g, dg) = |\langle\Psi_0(g+dg)|\Psi_0(g)\rangle|, \quad (2)$$

for small ($dg \rightarrow 0$) variations in g close to g_c . Therefore, by investigating the behavior of $F(g, dg)$ when couplings in the Hamiltonian are varied, one should be able to detect quantum criticality. Besides its novelty, this approach is purely quantum geometrical⁴ and therefore has the appeal that no *a priori* identification of order parameters is required.

The concept of *fidelity susceptibility*⁵ $\chi_F(g)$ naturally appears as the fidelity's leading term in the limit $dg \rightarrow 0$,

$$F(g, dg \rightarrow 0) \simeq 1 - \frac{1}{2}\chi_F(g)dg^2.$$

(The linear term in dg in the above expansion vanishes due to normalization of the wave-function — alternatively it can be seen to arise from the fact that $F(g, dg)$ is maximum at $dg = 0$ for any value of g .) The aforementioned drop in $F(g, dg)$ close to a QCP is thus associated to a divergence in χ_F and the latter quantity may also be employed in the study of quantum phase transitions. The situation here is reminiscent of the use of the specific heat to detect *thermal* phase transitions: while the presence of singularities in the specific heat for varying temperatures signals the location of finite-temperature critical points, $\chi_F(g)$ is a system's response to changes in the coupling constant g , whose divergencies are associated to the occurrence of *quantum* phase transitions.

Although obviously some information is lost in going from $F(g, dg)$ to $\chi_F(g)$, and for instance it is currently not clear whether transitions of order higher than second can be detected by studying the latter, focusing on $\chi_F(g)$ has up to now proved to be a fruitful strategy. The main reason behind this is that it is possible to show⁵⁻⁷ that $\chi_F(g)$ is closely related to more conventional physical quantities, such as imaginary-time dynamical responses. This is particularly advantageous since it allows one to rely on well established concepts and techniques from theoretical condensed-matter physics in order to draw conclusions on the properties of $\chi_F(g)$. We follow this line of reasoning in this paper, in a twofold way.

First, we present the details of a recently introduced⁸ quantum Monte Carlo (QMC) scheme that allows for the evaluation of χ_F for a large class of sign-problem-free models. This constitutes an important advance as the group of problems that can be studied within the fidelity approach is considerably enlarged, and additionally one benefits from the computational power of QMC methods. In particular, high-precision scaling analysis for models in dimensions higher than one is now possible: previous computations of χ_F for two-dimensional systems have relied on exact diagonalization (ED) techniques and were restricted to small system sizes, something that precludes

a precise determination of scaling dimensions in the vicinity of a QCP.

Second, by building upon the aforementioned relationship between χ_F and response functions, we determine the scaling behavior of the fidelity susceptibility close to a QCP. The divergence of $\chi_F(g)$ at g_c is shown to be related to the critical exponent ν describing the divergence of the correlation length. In this way, and supported by the results obtained from the QMC simulations, we assess the validity of other scaling analysis for the divergence of χ_F that have recently appeared in the literature.

Throughout the paper, we also analyze the properties of the ground-state energy's second derivative, $\partial^2 E_0(g)/\partial g^2$. This quantity is closely related to the fidelity susceptibility⁷ and, as explained in Sec. II C, scales in a way related to the scaling of χ_F in the quantum critical regime. Since the computation of $\partial^2 E_0(g)/\partial g^2$ within QMC is much more efficient than that of χ_F , as discussed in Sec. III B, it is important to address the question of which of these quantities is best suited to the study of second-order quantum phase transitions and of whether the current interest around the concept of fidelity susceptibility is justified on practical grounds.

The paper is organized as follows. After reviewing basic concepts in the fidelity approach in Sec. II A, we analyze an extension of the concept of fidelity susceptibility to finite temperatures (a prerequisite for path-integral QMC simulations) and relate it to a more commonly employed metric for thermal states in Sec. II B. We then perform a scaling analysis of χ_F and $\partial^2 E_0(g)/\partial g^2$ in Sec. II C and relate their scaling dimensions to conventional critical exponents.

In Sec. III, we give a detailed account of the previously introduced⁸ QMC scheme for calculating χ_F and further explore it (Sec. IV) in order to determine the scaling dimension of the fidelity susceptibility in one of the most paradigmatic models in the field of quantum phase transitions: the transverse-field Ising model (TIM) in two dimensions. Throughout the paper, concepts are illustrated by presenting results for the one-dimensional version of the TIM, which is exactly solvable.^{9–11} A summary is given in Sec. V and important technical details are discussed in the Appendix. Some of the results present in this paper have been first presented (by some of us) in Ref. 8.

II. FIDELITY SUSCEPTIBILITY

A. Definition

We consider the limit of $dg \rightarrow 0$ and perturbatively calculate the overlap appearing in Eq. (2) to leading order in dg . The fidelity susceptibility, defined by Eq. (I), can easily be shown to read^{4,5}

$$\chi_F(g) = \sum_{n \neq 0} \frac{|\langle \Psi_n(g) | H_1 | \Psi_0(g) \rangle|^2}{[E_n(g) - E_0(g)]^2}, \quad (3)$$

in terms of the eigenbasis

$$\sum_n |\Psi_n(g)\rangle \langle \Psi_n(g)| = I \quad (4)$$

of $\mathcal{H}(g)$, $\mathcal{H}(g)|\Psi_n(g)\rangle = E_n(g)|\Psi_n(g)\rangle$.

Starting from Eq. (3), one can relate^{5,6} $\chi_F(g)$ to the imaginary-time correlation function

$$G_{H_1}(\tau) = \theta(\tau) (\langle H_1(\tau) H_1(0) \rangle - \langle H_1 \rangle^2), \quad (5)$$

where $H_1(\tau) = e^{\tau \mathcal{H}} H_1 e^{-\tau \mathcal{H}}$, with τ denoting an imaginary time, $\theta(\tau)$ is the Heaviside step function and zero-temperature averages are defined by $\langle \mathcal{O} \rangle = \langle \Psi_0(g) | \mathcal{O} | \Psi_0(g) \rangle$. Inserting Eq. (4) into this last equation and taking its Fourier transform we arrive to

$$\tilde{G}_{H_1}(\omega) = \sum_{n \neq 0} \frac{|\langle \Psi_n(g) | H_1 | \Psi_0(g) \rangle|^2}{E_n(g) - E_0(g) + i\omega}, \quad (6)$$

The similarity between Eqs. (3) and (6) is evident and by simply performing a derivative, one can establish^{5,6} the important result

$$\chi_F(g) = i \left. \frac{d\tilde{G}_{H_1}(\omega)}{d\omega} \right|_{\omega=0} = \int_0^\infty d\tau \tau G_{H_1}(\tau). \quad (7)$$

This expression is remarkable for a number of reasons. First, it relates $\chi_F(g)$ to a dynamical response of the system to the “driving term” H_1 , evidencing its physical content. Second, as discussed in detail in Sec. II C, Eq. (7) allows us to address the issue of the scaling behavior of $\chi_F(g)$. Finally, Eq. (7) permits us to extend the definition of fidelity susceptibility to finite temperatures (Sec. II B) and therefore constitutes an obvious starting point in devising a scheme to obtain $\chi_F(g)$ from path-integral QMC simulations.

Before proceeding, it is also instructive to consider the ground-state energy's second-derivative, whose intimate relation to $\chi_F(g)$ has been pointed out in Refs. 7 and 12. Motivated by this close relationship, we define $\chi_E(g) = -\partial^2 E_0(g)/\partial g^2$ and, by using the eigenbasis of $\mathcal{H}(g)$, it is readily shown that

$$\chi_E(g) = -\frac{\partial^2 E_0(g)}{\partial g^2} = 2 \sum_{n \neq 0} \frac{|\langle \Psi_n(g) | H_1 | \Psi_0(g) \rangle|^2}{E_n(g) - E_0(g)}. \quad (8)$$

Comparing Eqs. (6) and (8) it is straightforward to see that

$$\chi_E(g) = 2\tilde{G}_{H_1}(\omega = 0) = 2 \int_0^\infty d\tau \tau G_{H_1}(\tau). \quad (9)$$

We can notice that the only important difference between Eqs. (3) and (8) is that in the former the denominator is squared: this is reflected by the appearance of the τ factor in Eq. (7), absent in Eq. (9). One might thus expect $\chi_F(g)$ to display a more pronounced behavior around a QCP and therefore to be a better indicator of quantum

criticality, an observation put onto firmer grounds by the scaling analysis of Sec. II C. Finally, similarly to the case of Eq. (7), the relation Eq. (9) can be used in order to extract $\chi_E(g)$ from QMC simulations, as we discuss in Sec. III B.

B. Finite Temperature

Before discussing how to extend the definition of fidelity susceptibility $\chi_F(g)$ to finite temperatures ($T = 1/\beta$) it is instructive to consider first the similar extension for $\chi_E(g)$. From Eq. (9), one obtains the finite- T generalization

$$\chi_E(g, \beta) = 2 \int_0^{\beta/2} G_{H_1}(\tau) d\tau, \quad (10)$$

where now $G_{H_1}(\tau)$ is still defined by Eq. (5) but with *thermal* averages, $\langle \mathcal{O} \rangle = Z^{-1} \text{Tr} [\exp(-\beta \mathcal{H}) \mathcal{O}]$ replacing ground-state expectation values [$Z = \text{Tr} \{\exp(-\beta \mathcal{H})\}$ is the partition function]. An important subtlety is apparent here: notice that the upper integration limit in the above expression is $\beta/2$, instead of β . The underlying reason is that, within the path-integral formalism used in QMC simulations, periodic boundary conditions are implied along the imaginary time direction. Connected physical correlation functions, such as $G_{H_1}(\tau)$, are periodic along the τ -direction, with period β . This is illustrated in Fig. 1(a) for the one-dimensional TIM (see Sec. IV A) on a chain with $L = 16$ sites and $\beta J = 16$, for $h/J = 1$: we see that $G_{H_1}(\tau)$ is symmetric around $\beta/2$ (vertical dashed line) and decays to zero at $\tau \rightarrow \beta/2$ for large enough β , a trend already noticeable in Fig. 1(a) where data for the relatively high temperature $\beta J = 16$ are displayed. Therefore, in the present case we have $\chi_E(g) = 2 \int_0^{\beta/2} G_{H_1}(\tau) d\tau = \int_0^{\beta} G_{H_1}(\tau) d\tau$.

The definition of fidelity susceptibility [Eq. (7)] can be extended to finite temperatures in a similar way

$$\chi_F(g, \beta) = \int_0^{\beta/2} \tau G_{H_1}(\tau) d\tau. \quad (11)$$

An important difference appears though: the aforementioned properties of $G_{H_1}(\tau)$ are *not* shared by the function $\tau G_{H_1}(\tau)$, since the pre-factor τ destroys the periodicity along the imaginary-time direction. This is illustrated in Fig. 1(b), again using the one-dimensional TIM as an example. In particular, $\int_0^{\beta/2} \tau G_{H_1}(\tau) d\tau \neq \int_{\beta/2}^{\beta} \tau G_{H_1}(\tau) d\tau$ and, therefore, in order to ensure that $\chi_F(g, \beta)$ converges correctly to its zero temperature limit, $\lim_{\beta \rightarrow \infty} \chi_F(g, \beta) = \chi_F(g)$, one must cut the integral at $\beta/2$. This has important implications for the QMC evaluation that is now made possible by Eq. (11), as clarified in Sec. III A.

While the just discussed generalization of χ_F to finite β [Eq. (11)] has been introduced for computational purposes, it is possible to relate it to more commonly used

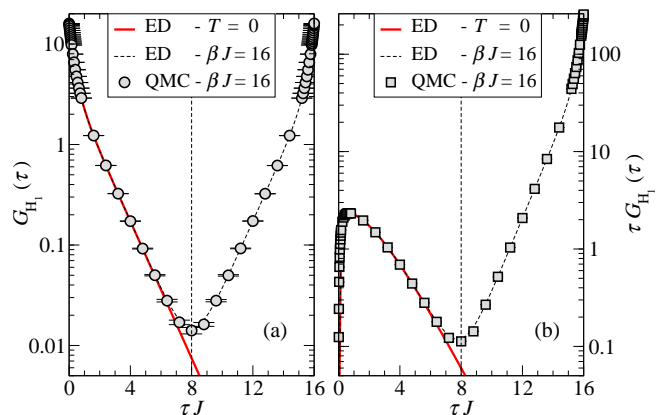


FIG. 1: (Color online) Correlation functions (a) $G_{H_1}(\tau)$ and (b) $\tau G_{H_1}(\tau)$, as a function of τ , for finite inverse temperature $\beta J = 16$ for the $d = 1$ TIM on a chain with $L = 16$ sites and $h/J = 1$ (see Sec. IV A). Data are generated by using the QMC method detailed in Sec. III and fixing the parity to the $P = +1$ sector (Sec. IV A 2). Exact Diagonalization (ED) data with fixed parity $P = +1$ are also shown both for finite and zero temperatures.

metrics for thermal (mixed) quantum states,¹³ as we discuss in what follows.

1. Bures Metric

The so-called Uhlmann fidelity generalizes the concept of fidelity [Eq. (2)] to the case of mixed states. For density matrices ρ_A and ρ_B , it is defined as¹⁴

$$\mathcal{F}(\rho_A, \rho_B) = \text{Tr} \sqrt{\rho_A^{1/2} \rho_B \rho_A^{1/2}},$$

and has an associated metric $ds(\rho_A, \rho_B) = \sqrt{2[1 - \mathcal{F}(\rho_A, \rho_B)]}$, known as the Bures distance. We are interested in the case of *thermal* density matrices,

$$\rho_g = \frac{1}{Z} \sum_n e^{-\beta E_n(g)} |\Psi_n(g)\rangle \langle \Psi_n(g)|,$$

expressed here in terms of the eigenbasis of $\mathcal{H}(g)$ [Eq. (4)]. The concept of fidelity susceptibility [Eq. (3)] can then be extended to the finite- T regime with the Bures metric $ds^2(g, \beta) = ds^2(\rho_g, \rho_{g+dg})$ for density matrices associated to infinitesimally close ($dg \rightarrow 0$) couplings in the Hamiltonian, g and $g + dg$. Following Zanardi *et al.*,¹³ one obtains the following expression for $ds^2(g, \beta)$ (for the sake of simplicity we omit the dependence on g of the eigenvalues and eigenvectors in the remainder of this Section)

$$ds^2(g, \beta) = ds_{\text{cl}}^2(g, \beta) + \sum_{n>m} \frac{|\langle \Psi_n | H_1 | \Psi_m \rangle|^2 e^{-\beta E_n} (1 - e^{-2x})^2}{(E_n - E_m)^2 Z (1 + e^{-2x})}, \quad (12)$$

where $x = \beta(E_m - E_n)/2$. One appealing feature in this expression is that it distinguishes “classical” and quantum contributions. The “classical” term, $ds_{\text{cl}}^2(g, \beta)$, is given by¹³

$$ds_{\text{cl}}^2(g, \beta) = \frac{\beta^2}{4} (\langle H_{1,\text{d}}^2 \rangle - \langle H_{1,\text{d}} \rangle^2). \quad (13)$$

Here, $H_{1,\text{d}}$ denotes the diagonal elements of H_1 in the eigenbasis Eq. (4), so that

$$\langle H_{1,\text{d}} \rangle = \frac{1}{Z} \sum_n e^{-\beta E_n} \langle \Psi_n | H_1 | \Psi_n \rangle.$$

$$\chi_{\text{F}}(g, \beta) = \frac{1}{Z} \sum_{n,m} \int_0^{\beta/2} d\tau \tau \left[e^{-\beta E_n + \tau(E_n - E_m)} |\langle \Psi_n | H_1 | \Psi_m \rangle|^2 - \frac{e^{-\beta(E_n + E_m)}}{Z} \langle \Psi_n | H_1 | \Psi_n \rangle \langle \Psi_m | H_1 | \Psi_m \rangle \right].$$

The terms with $n = m$ in the first term in the integrand are independent of τ and can be regrouped with the second term to yield $\frac{1}{2} ds_{\text{cl}}^2(g, \beta)$. Performing the integration for the remaining terms, we finally obtain

$$\chi_{\text{F}}(g, \beta) = \frac{ds_{\text{cl}}^2(g, \beta)}{2} + \sum_{n>m} \frac{|\langle \Psi_n | H_1 | \Psi_m \rangle|^2}{(E_n - E_m)^2} \frac{e^{-\beta E_n}}{Z} (1 - e^{-x})^2, \quad (14)$$

where again we set $x = \beta(E_m - E_n)/2$. One can readily show that in the limit $T \rightarrow 0$ both $\chi_{\text{F}}(g, \beta)$ [Eq. (14)] and $ds^2(g, \beta)$ [Eq. (12)] converge to the ground-state result of Eq. (3), as desired. This is illustrated for the TIM on the square lattice in Fig. 3, where data from QMC [for $\chi_{\text{F}}(g, \beta)$] and exact diagonalizations [for both $\chi_{\text{F}}(g, \beta)$ and $ds^2(g, \beta)$] are displayed (see discussion in Sec. IV B). On the other hand, the high-temperature limit ($\beta \rightarrow 0$) yields $ds^2(g, \beta \rightarrow 0) = 2\chi_{\text{F}}(g, \beta \rightarrow 0) = \frac{\beta^2}{4} (\langle H_1^2 \rangle - \langle H_1 \rangle^2)$.

In order to analyze the general case, we evaluate the ratio between $f(x) = (1 - e^{-2x})^2 / (1 + e^{-2x})$, that appears in Eq. (12), and $g(x) = (1 - e^{-x})^2$ [from Eq. (14)]. We have $f(x)/g(x) = 1 + 1/\cosh(x)$ and therefore $f(x)/2 \leq g(x) \leq f(x)$. Noting that $ds_{\text{cl}}^2(g, \beta) \geq 0$, we can conclude that

$$\frac{1}{2} ds^2(g, \beta) \leq \chi_{\text{F}}(g, \beta) \leq ds^2(g, \beta). \quad (15)$$

These inequalities show that if $ds^2(g, \beta)$ diverges, then $\chi_{\text{F}}(g, \beta)$ must also diverge and we conclude that both quantities are equally well suited for detecting criticality. While in this paper we are interested in quantum phase transitions and thus focus on the limit $\beta \rightarrow \infty$, it would also be of interest to investigate the finite- T behavior of $\chi_{\text{F}}(g, \beta)$: as discussed in Ref. 13, this quantity might be able to detect thermal phase transitions and/or finite- T signatures of quantum criticality.

On the other hand, the second term in Eq. (12) is of pure quantum origin and vanishes unless $[\rho_g, \rho_{g+dg}] \neq 0$.¹³

2. Relation between $\chi_{\text{F}}(g, \beta)$ and $ds^2(g, \beta)$

We now relate the two previously discussed finite temperature extensions for the fidelity susceptibility, namely Eqs. (11) and (12, 13). We expand the trace for thermal averages and insert the eigenbasis of $\mathcal{H}(g)$ [Eq. (4)] in Eq. (11) arriving to

C. Scaling Behavior

We focus now on the issue of how the fidelity susceptibility χ_{F} behaves in the vicinity of a QCP and start by reviewing the main results from the scaling analysis devised by Campos Venuti and Zanardi.⁶

Starting from Eq. (7) and following standard scaling arguments (see for instance Ref. 15), they apply the scale transformation $x' = sx$, $\tau' = s^z \tau$ (z is the dynamic critical exponent), and arrive to the following relation for the scaling of the fidelity susceptibility density:

$$L^{-d} \chi_{\text{F}} \sim |g - g_c|^{\nu(d+2z-2\Delta_{H_1})}. \quad (16)$$

Here, $L^d = N$ is the number of sites for a d -dimensional system. In what follows, we assume that a second-order quantum phase transition takes place at a value g_c of the “driving parameter” g and that the correlation length diverges in its neighborhood as $\xi \sim |g - g_c|^{-\nu}$; Δ_{H_1} is the scaling dimension of the driving term H_1 in Eq. (1): $H_1' = s^{-\Delta_{H_1}} H_1$. Standard finite-size scaling arguments thus imply that

$$\chi_{\text{F}} \sim L^{-2(z-\Delta_{H_1})} \quad (17)$$

for finite systems at criticality.

An alternative scaling analysis has been recently put forward by some of us in Ref. 8, where the simpler result

$$\chi_{\text{F}} \sim L^{2/\nu}, \quad (18)$$

has been derived. The appeal of the above scaling relation, as compared to Eq. (17), stems from the fact that it is not expressed in terms of the exponent Δ_{H_1} , rarely dealt with in more conventional approaches to quantum critical phenomena. In fact, Δ_{H_1} can easily be related to the exponent ν (see Ref 8). In what follows, we provide an intuitive equivalent derivation of the result Eq. (18).

We start by remarking that at $T = 0$ the free-energy density f_H reduces to the ground-state energy density, $L^{-d}E_0$. Since, by definition, $f_H \sim |g - g_c|^{2-\alpha}$ (see for instance Ref. 15), one readily obtains

$$L^{-d}\chi_E \sim |g - g_c|^{-\alpha}. \quad (19)$$

This relation is not at all surprising since, as we can see from Eq. (9), $\chi_E(g) = -\partial^2 E_0(g)/\partial g^2$ is similar to a “zero-temperature specific heat”. Comparing the expressions for χ_E [Eq. (9)] and χ_F [Eq. (7)], one sees that the only difference is the presence of an imaginary time (or inverse energy) scale τ in the latter, that we naturally expect to scale as $|g - g_c|^{-z\nu}$ in the critical regime.¹⁵ We thus arrive at

$$L^{-d}\chi_F \sim |g - g_c|^{-(\alpha+z\nu)} = |g - g_c|^{-(2-d\nu)}, \quad (20)$$

where we have made use of the hyper-scaling formula $2 - \alpha = \nu(d + z)$. Therefore, we arrive to the conclusion that $L^{-d}\chi_F$ diverges only when $\nu < 2/d$.

On the other hand, by similarly inserting the hyper-scaling formula into Eq. (19), we obtain $L^{-d}\chi_E \sim |g - g_c|^{-2+\nu(d+z)}$ and, as anticipated in Sec. II A, conclude that χ_E has a weaker divergence than χ_F at a critical point. Furthermore, we find that the more stringent condition $\nu < 2/(d + z)$ must be satisfied for $L^{-d}\chi_E$ to diverge and that there might be situations where only $L^{-d}\chi_F$ displays a divergence at a critical point, being in general a better indicator of quantum criticality.

Next, by performing a finite-size scaling analysis, we conclude that for the fidelity susceptibility per site we have

$$L^{-d}\chi_F \sim L^{\frac{2}{\nu}-d}, \quad (21)$$

in agreement with the result Eq. (18) (Ref. 8). For $L^{-d}\chi_E$, we similarly obtain

$$L^{-d}\chi_E \sim L^{\frac{2}{\nu}-(d+z)}. \quad (22)$$

The validity of the scaling relations Eqs. (21) and (22) is confirmed by the analysis of the QMC data performed in Sec. IV C. Finally, we note that the scaling relations presented here have been independently found in the context of quantum quenches,^{16–18} as discussed in Sec. V.

III. STOCHASTIC SERIES EXPANSION

Despite the sign problem that precludes efficient simulations of most fermionic/frustrated models, Quantum Monte Carlo methods are among the most efficient tools to simulate quantum many-body problems. Particularly useful for our purpose here is the QMC formulation known as *Stochastic Series Expansion* (SSE), developed by Sandvik and coworkers.^{19–21} Basically (for a detailed account the reader is referred to Ref. 21), SSE relies on a power series expansion of the system’s partition

function²²

$$Z = \text{Tr} (e^{-\beta\mathcal{H}}) = \sum_{n=0}^{\infty} \sum_{\alpha} \sum_{S_n} \frac{\beta^n}{n!} \left\langle \alpha \left| \prod_{i=1}^n \mathcal{H}(b^i) \right| \alpha \right\rangle. \quad (23)$$

Here $\{|\alpha\rangle\}$ is any suitable basis and the system’s Hamiltonian is typically a sum over local operators: $\mathcal{H} = \sum_b \mathcal{H}(b)$, with b labeling different local terms. For instance, b may denote operators acting on different bonds of the lattice and/or diagonal versus non-diagonal operators. For our current purposes, it is convenient to choose a decomposition that respects the bipartition of Eq. (1), such that all terms appearing in H_0 are labelled by b_0 and those appearing in gH_1 by b_1 and we have $b \in \{b_0, b_1\}$. SSE configurations (α, S_n) , with operator strings

$$S_n = \prod_{i=1}^n \mathcal{H}(b^i), \quad (24)$$

are then sampled, according to the statistical weight

$$W(\alpha, S_n) = \frac{\beta^n}{n!} \left\langle \alpha \left| \prod_{i=1}^n \mathcal{H}(b^i) \right| \alpha \right\rangle.$$

Efficient update schemes such as the *directed loop* algorithm^{21,23} render the SSE technique one of the most efficient QMC methods for quantum lattice models.

The general procedure for obtaining thermal averages within the SSE framework is discussed in detail by Sandvik in Ref. 24. The basic idea, supposing we are interested in an observable \mathcal{O} , is to determine an *estimator* $O(\alpha, S_n)$ such that

$$\langle \mathcal{O} \rangle_W = \frac{1}{Z} \sum_n \sum_{(\alpha, S_n)} O(\alpha, S_n) W(\alpha, S_n).$$

In what follows, we show how estimators for the fidelity susceptibility $\chi_F(g, \beta)$ [Eq. (11)] and $\chi_E(g, \beta)$ [Eq. (10)] can be obtained from SSE QMC simulations.

A. Fidelity Susceptibility

First, we need to evaluate imaginary-time operator products of the form $\langle H_1(\tau)H_1(0) \rangle$ appearing in the integrand of Eq. (11) [cf. Eq. (5)]. These operators being part of the Hamiltonian, one trick consists in re-interpreting two of the elements with label b_1 of the string Eq. (24) as the operators to be measured. Following Ref. 24, we arrive to

$$g^2 \langle H_1(\tau)H_1(0) \rangle = \sum_{m=0}^{n-2} \frac{(n-1)!}{(n-m-2)!m!} \beta^{-n} (\beta - \tau)^{n-m-2} \tau^m \langle N_{gH_1}(m) \rangle_W. \quad (25)$$

Here, n is the length of the operator string S_n [Eq. (24)] and $N_{gH_1}(m)$ the number of times any two operators

comprising gH_1 appear in the strings S_n separated by m positions. We discuss below how $N_{gH_1}(m)$ can be measured.

The second term in Eq. (5) is obtained by a simpler procedure²⁴ and is given by

$$\langle H_1 \rangle^2 = \frac{1}{g^2 \beta^2} \langle N_{gH_1} \rangle_W^2, \quad (26)$$

where N_{gH_1} is the total number of gH_1 operators in S_n .

Inserting the results Eqs. (25, 26) into Eq. (11) and integrating from $\tau = 0$ to $\beta/2$ (taking into account the important multiplicative factor of τ in the integrand), we finally arrive to the result

$$\chi_F(g, \beta) = \frac{1}{g^2} \sum_{m=0}^{n-2} [A(m, n) \langle N_{gH_1}(m) \rangle_W] - \frac{\langle N_{gH_1} \rangle_W^2}{8g^2}, \quad (27)$$

with the coefficient

$$A(m, n) = \frac{(n-1)!}{(n-m-2)!m!} \int_0^{1/2} d\tau \tau^{m+1} (1-\tau)^{n-m-2}. \quad (28)$$

We show in Appendix A how this coefficient can be approximated very accurately by an analytical expression in the limit of $n \gg 1$.

$N_{gH_1}(m)$ is conveniently extracted from the simulations in two steps. Firstly, the string Eq. (24) is traversed (for instance when performing diagonal updates; see Ref. 19) and the positions i where a local Hamiltonian $\mathcal{H}(b^i)$ appears with a label $b^i = b_1$ are recorded (there are in total N_{gH_1} such operators). Secondly, the histogram $N_{gH_1}(m)$ is generated by computing all distances m between all previously recorded positions i . This step is the most demanding as it requires $N_{gH_1}(N_{gH_1} - 1)/2$ operations. Note finally that the prefactor $1/g^2$ arises from the definition of the fidelity susceptibility Eq. (3) which does not include the coupling constant g , whereas the SSE decomposition used in Eq. (23) typically does.

B. Ground-State Energy's Second Derivative

The results Eqs. (25, 26) can also be used in order to directly evaluate the ground-state energy's second derivative, relying on Eq. (10) and extrapolating to the limit $\beta \rightarrow \infty$. The absence of the factor τ in Eq. (9) considerably simplifies the situation since the integration over τ can now always be performed exactly. In this way, we arrive to the simple result

$$\chi_E(g, \beta) = \frac{1}{g^2 \beta} \left[\langle N_{gH_1}^2 \rangle_W - \langle N_{gH_1} \rangle_W^2 - \langle N_{gH_1} \rangle_W^2 \right]. \quad (29)$$

We stress that the computational cost for evaluating $\chi_E(g, \beta)$ is much lower than the one required to obtain $\chi_F(g, \beta)$: the estimator for the former quantity in Eq. (29) simply requires counting the number of times the operators contained in the “driving term” gH_1 occur

in the operator strings S_n . This is to be contrasted with the computationally heavy task, specially in the limit of large lattice sizes and low temperatures, of computing the histogram $N_{gH_1}(m)$ necessary in evaluating $\chi_F(g, \beta)$ [cf. Eqs. (27, 28)].

IV. NUMERICAL SIMULATIONS

A. Transverse-Field Ising Model

1. Definition

The transverse-field Ising model (TIM) is perhaps the simplest model to display a QCP and many key concepts in the theory of quantum critical phenomena have been developed by analyzing its properties.²⁵

The TIM Hamiltonian reads

$$\mathcal{H}(h) = JH_J + hH_h = -J \sum_{\langle i,j \rangle} \sigma_i^x \sigma_j^x - h \sum_i \sigma_i^z, \quad (30)$$

where $\langle i, j \rangle$ denotes nearest-neighbor sites on a d -dimensional lattice and $\sigma_i^{x,z}$ are Pauli matrices attached to the site i . We set the energy scale by henceforth fixing $J = 1$.

At zero temperature and in any dimension, a quantum phase transition occurring at a field h_c separates a ferromagnetic phase for low fields $h < h_c$ from a polarized one for $h > h_c$, with spins aligning along the field direction. The quantum phase transition in d dimensions belongs to the universality class of the finite-temperature phase transition of the classical Ising model in $d+1$ dimensions and has a dynamic critical exponent $z = 1$.²⁵

The TIM is exactly solvable in the one-dimensional case.⁹⁻¹¹ The QCP is located at $h_c = 1$ and most observables, including χ_F ,³ can be computed analytically. We make use of these exact results in establishing the validity of the QMC method discussed in Sec. III, for instance in Sec. IV A 2, where the issue of parity is discussed. On the other hand, the TIM is not solvable in two dimensions and has been investigated mainly through means of numerical techniques.²⁶⁻³¹ The most precise estimate for the location of the QCP, $h_c = 3.04438(2)$, has been obtained from a QMC approach.³¹

Before proceeding, we remark that a scaling analysis for the fidelity susceptibility and the second derivative of the ground-state energy for the TIM on the square lattice has been recently performed by Yu and collaborators in Ref. 32. Results are compared in Sec. V.

2. Parity quantum number

An important issue concerning the TIM is the existence of a conserved quantum number, the parity P . It

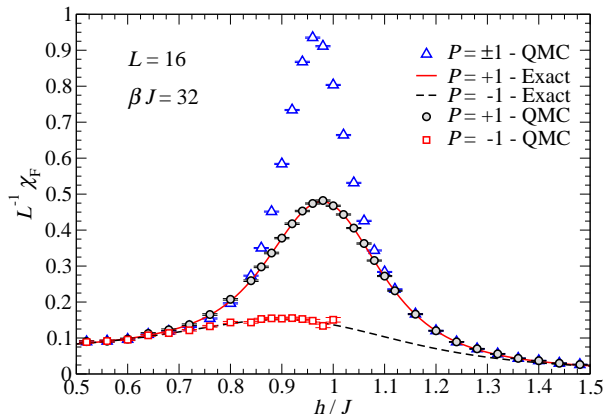


FIG. 2: (Color online) Fidelity susceptibility density for the 1d TIM, as obtained from the exact solution (curves) and QMC simulations (symbols; see Sec. III A). Results for both parity sectors $P = -1$ and $+1$ are shown (see Sec. IV A 2). QMC results indicated by $P = \pm 1$ (triangles) have been obtained by making no distinction between parity sectors. For $h/J \gtrsim 1$, statistics are insufficient to estimate χ_F in the $P = -1$ sector from QMC simulations since only the ground-state in the $P = +1$ sector is sampled at the low temperature considered here, $\beta J = 32$. Data are for a system of size $L = 16$ with periodic boundary conditions.

is readily verified that the parity operator,

$$\mathcal{P} = \prod_{i=1}^N \sigma_i^z \quad (31)$$

(for a system with N sites), commutes with the TIM Hamiltonian Eq. (30), $[\mathcal{H}, \mathcal{P}] = 0$, and therefore the parity $P = \pm 1$ is a good quantum number.

For finite systems, the ground-state of the TIM lies in the $P = +1$ sector, as shown by the following argument. It is convenient to work in the basis given by tensor products of the eigenvectors $\{|\uparrow\rangle_x, |\downarrow\rangle_x\}$ of σ_i^x at every site: $\{|\phi_m\rangle\}$ with, for instance, $|\phi_m\rangle = |\uparrow\downarrow\downarrow\uparrow \dots\rangle_x$. All off-diagonal matrix elements for the Hamiltonian Eq. (30) are non-positive in this basis and therefore the TIM on *finite lattices* satisfies the conditions for the Perron-Frobenius theorem to apply. According to this theorem, the coefficients of the system's ground-state (in its expansion in terms of the basis $\{|\phi_m\rangle\}$, $|\Psi_0\rangle = \sum_m c_m |\phi_m\rangle$) must all have the same sign (say, $c_m \geq 0$). Consider the lowest-lying states in each parity sector $|\Psi_0^\pm\rangle$: they can be expanded as $|\Psi_0^\pm\rangle = \sum_m c_m^\pm |\phi_m^\pm\rangle$, with $\{|\phi_m^\pm\rangle\}$ denoting the subset of elements in $\{|\phi_m\rangle\}$ with fixed parity $P = \pm 1$. The argument proceeds by noticing that the parity operator [Eq. (31)] simply acts as a spin reversal operator upon the elements of the σ^x basis: namely, $\mathcal{P}|\phi_m^\pm\rangle = |\psi_m^\pm\rangle$, where $|\psi_m^\pm\rangle$ is obtained from $|\phi_m^\pm\rangle$ by flipping all spins (for instance, $\mathcal{P}|\uparrow\downarrow\downarrow\uparrow \dots\rangle_x = |\downarrow\uparrow\uparrow\downarrow \dots\rangle_x$). Thus, the expression

$$\mathcal{P}|\Psi_0^\pm\rangle = \sum_m c_m^\pm \mathcal{P}|\phi_m^\pm\rangle = \sum_m c_m^\pm |\psi_m^\pm\rangle = \pm |\Psi_0^\pm\rangle,$$

is only consistent with the positiveness of the ground-state if $P = +1$ (one readily sees that the above relation can only be satisfied in the $P = -1$ sector if the coefficients for the basis elements $|\phi_n^\pm\rangle$ and $\mathcal{P}|\phi_n^\pm\rangle = |\psi_n^\pm\rangle$ have opposite signs in the expansion for $|\Psi_0^\pm\rangle$).

The above discussion is directly relevant for our purposes here since, while expectation values for most physical observables are the same for the lowest-lying states in both parity sectors, this turns out *not* to be the case for χ_F and χ_E . This is illustrated in Fig. 2, where exact results for χ_F (curves, see Ref. 3) for the TIM on a chain with $L = 16$ sites are shown for both parities, $P = +1$ and $P = -1$. Also shown are data obtained from a naive QMC implementation not discriminating between different parity sectors (triangles in Fig. 2): the disagreement is evident, specially in the neighborhood of the QCP at $h_c = 1$. While we expect this discrepancy to disappear in the thermodynamic limit (as suggested by exact results for the $d = 1$ TIM for increasingly larger systems; however, we have no general proof), QMC simulations are obviously restricted to finite system sizes and it thus important to take the parity quantum number into account.

Fortunately, the parity of a given SSE configuration (α, S_n) can easily be determined within the here adopted convention for the TIM [Eq. (30)].³³ Indeed, the parity operator, defined in Eq. (31), is diagonal in the σ^z basis employed in SSE-QMC simulations and the parity is then readily obtained as

$$P = \prod_{i=1}^N \sigma_i^z |\alpha(\tau = 0)\rangle$$

(since the parity is a conserved number, it can be computed at any time-slice, in particular at $\tau = 0$). Both parity sectors are sampled due to the non-local updates in the QMC scheme (see Ref. 21). Therefore, our strategy consists in computing the estimators required for obtaining χ_F and χ_E (see Sec. III) for all SSE configurations (α, S_n) and storing the results in different variables according to the parity of the state $|\alpha(\tau = 0)\rangle$. Data obtained in this way for the $d = 1$ TIM are shown in Fig. 2 and perfectly agree with the exact results. Finally, since for finite systems the ground-state has $P = +1$, all results discussed in the present work have been obtained for this parity sector (with the exception of the indicated ones in Fig. 2).

B. Simulation Details

The computation of $\chi_F(g, \beta)$ and $\chi_E(g, \beta)$ requires only small changes to an existing SSE code: estimators for both quantities [Eqs. (27) and (29), respectively] are simply computed by analyzing the operator strings [Eq. (24)], a task ideally carried out while performing diagonal updates for the SSE configurations (α, S_n) .²¹ Our code is based on the ALPS³⁴ libraries implementation

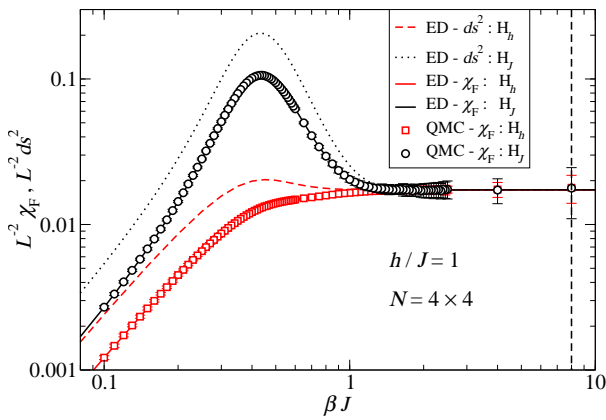


FIG. 3: (Color online) Finite- T fidelity susceptibility $L^{-2}\chi_F(g, \beta)$ [Eqs. (11,14)] and Bures metric $L^{-2}ds^2(g, \beta)$ [Eq. (12)] as a function of the inverse temperature $\beta = T^{-1}$ for the TIM on the square lattice ($N = 4 \times 4$ sites cluster with periodic boundary conditions; restriction to the $P = +1$ parity sector, see Sec. IV A 2). Both H_J and hH_h [see Eq. (30)] have been considered as the “driving term” H_1 in the definitions for $\chi_F(g, \beta)$ and $ds^2(g, \beta)$: we see that different choices yield the same $T = 0$ result. The vertical dashed line marks the value $\beta = 2L$ set in obtaining the QMC data displayed in Figs. 2 and 4: while for the coupling considered here ($h/J = 1$) the system is deep into the ferromagnetic phase and convergence to ground-state expectation values is achieved for smaller β , the more stringent condition $\beta = 2L$ is necessary closer to the QCP.

of SSE QMC.²³ The main modifications of the original codes are independent from measurements for χ_F and χ_E and are specific to the TIM [as defined by Eq. (30)] studied in the present work. They involve changes in the processes that are allowed when performing off-diagonal updates³⁵ and the computation of the parity quantum number (see Sec. IV A 2).

Calculating χ_F can be computationally demanding due to the fact that the number of operations required for obtaining the histogram $N_{gH_1}(m)$ [see Eq. (27)] scales quadratically with the total number of gH_1 operators in the string S_n . The situation can be ameliorated by a judicious bipartition of the system’s Hamiltonian into H_0 and H_1 [Eq. (1)].

Indeed, there is freedom to consider either H_J or hH_h (or, in general, any combination of these) appearing in Eq. (30) as the “driving term” H_1 in Eq. (3): since $\langle \Psi_n(h) | (H_J + hH_h) | \Psi_0(h) \rangle = 0$ for $n \neq 0$, we readily conclude from Eq. (3) that $\chi_F^{H_J} = h^2 \chi_F^{hH_h}$ (superscripts indicate the term assigned to H_1) and therefore different bipartition choices lead to the same zero-temperature results for χ_F , apart from a trivial multiplicative factor. Although this is no longer true for the finite- T generalizations of Eqs. (12) and (14),³⁶ the equivalence between results obtained from different partitions is recovered in the limit $T \rightarrow 0$, as shown in Fig. 3 for the TIM on the square lattice (data obtained from QMC simulations for

a 4×4 cluster and $h/J = 1$).

We may thus explore the fact that different terms in the Hamiltonian dominate in different regions of the phase diagram in order to reduce computational cost. Specifically, for the case of the TIM considered here [Eq. (30)] it is more efficient to compute $N_{gH_1}(m)$ in the high-field limit if we set $H_1 = H_J$, since the number of such operators in the strings S_n will be smaller than that of H_h operators in this limit. In practice, we find that, for field magnitudes close to the QCP for the TIM on the square lattice, setting $H_1 = H_J$ is the most efficient choice.

Following this strategy, we have simulated the TIM on the square lattice by considering clusters with linear size L and periodic boundary conditions (PBC), and are able to reach $L = 28$ when computing χ_F . On the other hand, computing χ_E requires much lesser numerical effort and we are able to reach $L = 48$. For both quantities, we find that if we set the inverse temperature $\beta = 2L$ both χ_F and χ_E reach their ground-state expectation values. This is illustrated in Fig. 3 for the $L = 4$ cluster. We have also performed a few simulations setting $\beta = 4L$ in order to confirm that convergence has indeed been achieved, at least within error bars, for $\beta = 2L$.

C. Results

Our QMC data for $L^{-2}\chi_F$ and $L^{-2}\chi_E$ for the TIM on the square lattice are shown in Fig. 4 for various system sizes L . The presence of peaks in the curves for both quantities is evident: they become more pronounced for increasing L and their positions seemingly converge toward the estimate $h_c = 3.04438(2)$ for the QCP found in Ref. 31 (see below). Furthermore, we notice that χ_E displays less pronounced peaks than χ_F , as expected from our discussion in Sec. II C. A quantitative data analysis is explained in what follows.

We start by determining the peaks positions and heights for both χ_F and χ_E from the raw data displayed in Fig. 4. The so obtained results are shown in Fig. 5. From the scaling relations derived in Sec. II C, $L^{-d}\chi_F \sim L^{\frac{2}{\nu}-d}$ and $L^{-d}\chi_E \sim L^{\frac{2}{\nu}-(d+z)}$ [Eqs. (21) and (22); $d = 2$ and $z = 1$], we expect a linear dependence for the logarithm of the peaks’ height on $\ln L$. This is confirmed by the results shown in Figs. 5(a) and (c). By applying linear regression to the points associated to the three largest values of L in each plot we obtain our first estimates for correlation length’s exponent: $\nu = 0.623(8)$ [χ_F , Fig. 5(a)] and $\nu = 0.615(1)$ [χ_E , Fig. 5(c)]. While the former estimate is in good agreement with the result for the universality class of the three-dimensional classical Ising model [$\nu = 0.6301(8)$, Ref. 37], the latter clearly underestimates ν . This is likely to be explained by the weak divergence displayed by χ_E , implying that regular sub-leading corrections are important in accounting for the behavior in system sizes as the ones considered here: indeed we notice that the data points corresponding to the smallest

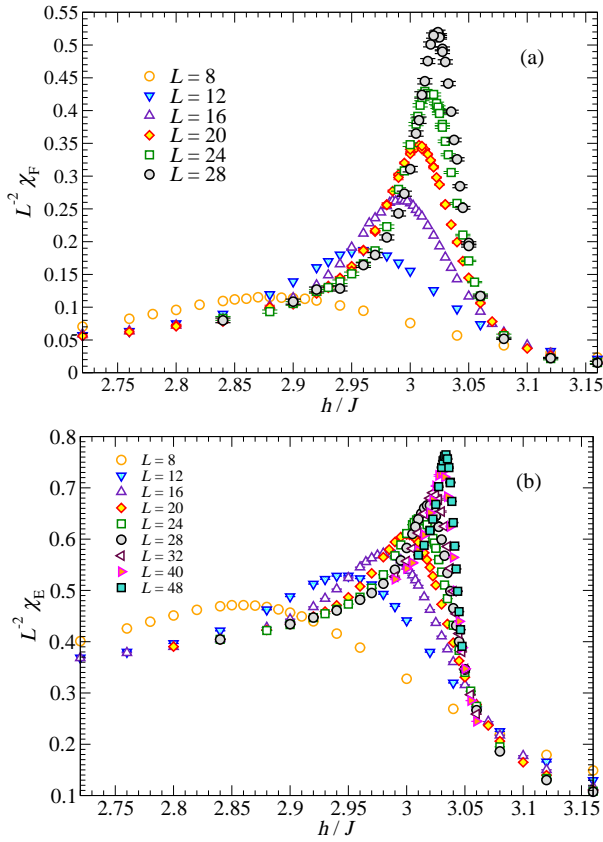


FIG. 4: (Color online) (a) Fidelity susceptibility density $L^{-2} \chi_F$ and (b) ground-state energy's second derivative per site $L^{-2} \partial^2 E_0(g) / \partial g^2 = -L^{-2} \chi_E(g)$ for the TIM on the square lattice, as a function of h/J and for indicated system sizes L (temperatures are set to $\beta = 2L$). Data have been obtained by applying the SSE QMC procedure detailed in Sec. III.

system sizes clearly deviate from the linear fit obtained for the points for the three largest L in Fig. 5(c).

In Figs. 5(b) and (d) we plot the peaks' location versus inverse system size $1/L$ for χ_F and χ_E , respectively. We expect (see for instance the related discussion in Ref. 38) the following expression to hold for the scaling of the peak positions for $h_c(L)$ with system size L

$$h_c(L) = h_c^\infty + \frac{\lambda}{L^{1/\nu}}, \quad (32)$$

where h_c^∞ is the result for $L \rightarrow \infty$. Data fits give the following estimates: $h_c^\infty = 3.0442(4)$ and $\nu = 0.625(7)$ [χ_F , Fig. 5(b)] and $h_c^\infty = 3.0442(7)$ and $\nu = 0.63(1)$ [χ_E , Fig. 5(d)]. We remark that our estimates for the location of the QCP are in very good agreement with the result from Ref. 31 and, although quality is lesser in this case, our results for ν are consistent with the value $\nu = 0.6301(8)$ found in Ref. 37.

Finally, from the finite size scaling analysis performed in Sec. II C we expect the following relation to describe the behavior of χ_F on finite systems in the neighborhood

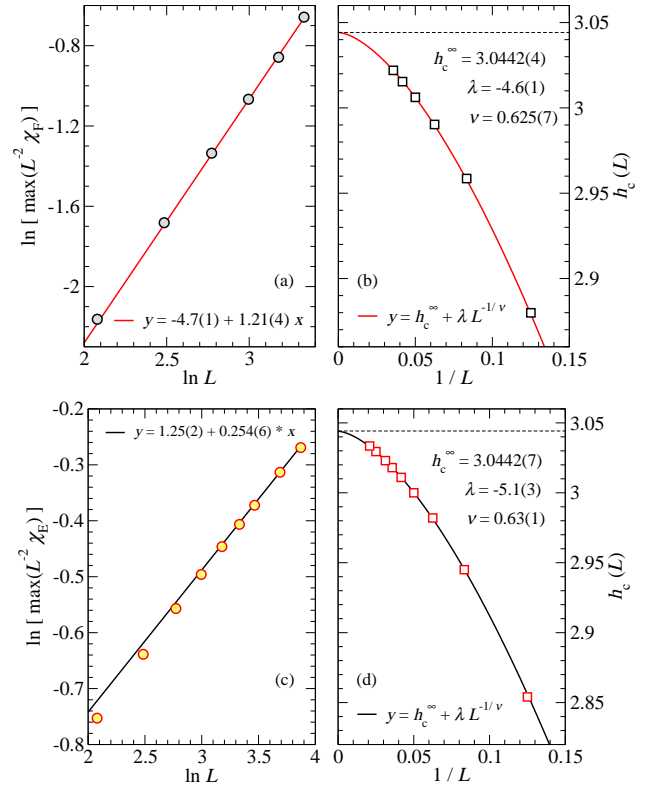


FIG. 5: (Color online) Finite size scaling analysis for the location and height of the peaks in χ_F [(a) and (b)] and χ_E [(c) and (d)], obtained from the QMC data shown in Fig. 4. In panels (a) and (c), the logarithm of the maxima in $L^{-2} \chi_F$ and $L^{-2} \chi_E$, respectively, are plotted as function of $\ln L$. Linear regression (lines) is applied to the three rightmost data-points in each case, yielding the estimates (a) $\nu = 0.623(8)$ and (c) $\nu = 0.615(1)$ for the correlation length's critical exponent. In (b) and (d), the peaks' location $h_c(L)$ for, respectively, $L^{-2} \chi_F$ and $L^{-2} \chi_E$ are plotted against inverse system size $1/L$. Fits (curves) for these results by using Eq. (32) yield the estimates: (b) $h_c^\infty = 3.0442(4)$ and $\nu = 0.625(7)$ and (d) $h_c^\infty = 3.0442(7)$ and $\nu = 0.63(1)$ (the extrapolated values h_c^∞ are indicated by the horizontal dashed lines). See main text for details.

of the QCP

$$L^{-d} \chi_F(h, L) = L^{\frac{2}{\nu} - d} f_{\chi_F} \left(L^{1/\nu} |h - h_c| \right), \quad (33)$$

and similarly for χ_E

$$L^{-d} \chi_E(h, L) = L^{\frac{2}{\nu} - (d+z)} f_{\chi_E} \left(L^{1/\nu} |h - h_c| \right). \quad (34)$$

In the above expressions f_{χ_F} and f_{χ_E} are homogeneous functions, *a priori* unknown. Estimates for critical parameters can thus be obtained by plotting $L^{-\frac{2}{\nu}} \chi_F$ and $L^{-\frac{2}{\nu} + z} \chi_E$ versus $L^{1/\nu} |h - h_c|$ and adjusting the values of h_c and ν until data collapse is achieved. The so obtained data collapse plots are displayed in Fig. 6, from which we get the following estimates: $h_c = 3.0440(15)$ and $\nu = 0.625(3)$ [χ_F , Fig. 6(a)], and $h_c = 3.044(2)$ and

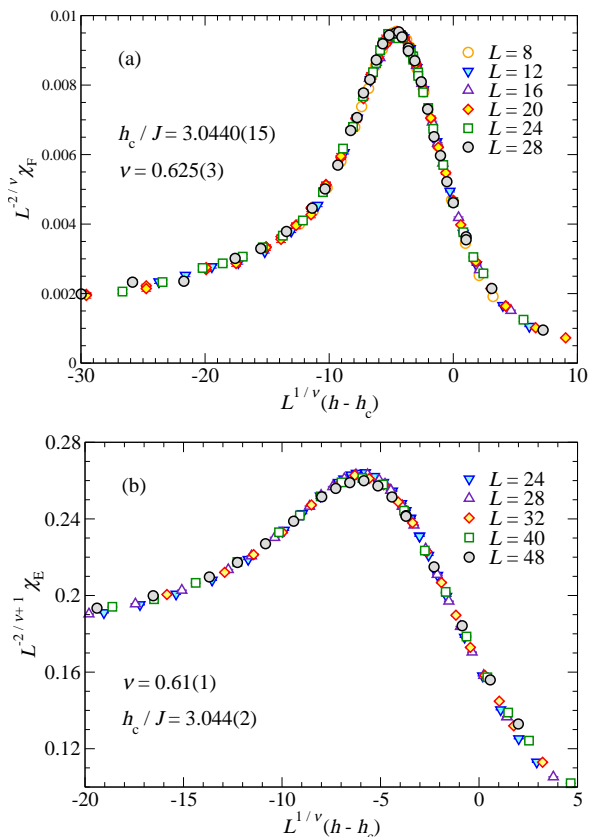


FIG. 6: (Color online) (a) Data collapse for the QMC results for $L^{-2}\chi_F$ (a) and $L^{-2}\chi_E$ (b) for the TIM on the square lattice and indicated system sizes. Data collapse is achieved for: (a) $h_c = 3.0440(15)$ and $\nu = 0.625(3)$ and (b) $h_c = 3.044(2)$ and $\nu = 0.61(1)$. In panel (b), data for the smallest system sizes are discarded (see main text).

$\nu = 0.61(1)$ [χ_E , Fig. 6(b)]. All of these values are in agreement with published results [$h_c = 3.04438(2)$ from Ref. 31 and $\nu = 0.6301(8)$, Ref. 37], but we remark the slightly lesser quality of the data collapse achieved for χ_E . Indeed, data obtained from the smallest system sizes in Fig. 4(b) fail to collapse onto the curve for the largest L in Fig. 6(b) and have not been taken into account when performing the analysis. Again, we believe that this is explained by the weakly divergent behavior of χ_E .

V. DISCUSSION AND CONCLUSIONS

In summary, we have investigated the scaling properties of the fidelity susceptibility χ_F in the quantum critical regime. Large scale quantum Monte Carlo simulations for the transverse-field Ising model on the square lattice, performed by using the scheme introduced in Ref. 8, confirm the validity of the derived scaling relations. Additionally, we also investigate the scaling behavior of the ground-state energy's second derivative, $\partial^2 E_0(g)/\partial g^2 = -\chi_E(g)$, a quantity closely related to χ_F .

We would like to highlight the fact that the novel QMC scheme for computing χ_F presented in Ref. 8 and discussed in detail in the present work opens several research possibilities within the so-called fidelity approach to quantum critical phenomena. Indeed, investigations in this field have been so far, to a large extent, restricted to one-dimensional systems, while our QMC scheme allows for the study of χ_F for a large class of sign-problem-free models in arbitrary dimensions. Furthermore, we stress that the required modifications in a pre-existing SSE code are minimal and that, even though SSE is particularly well suited for the task, it is also likely that measurements for $\chi_F(g)$ can be implemented within other QMC flavors, such as the loop algorithm.³⁹ Another potentially interesting possibility opened by the QMC method considered here involves the study of the finite- T properties of χ_F (which scales as the Bures metric, as shown in Sec. II B), along the lines of Ref. 13.

A second point worth to emphasize is the particularly simple scaling relations for χ_F derived in Sec. II C, expressed *solely* in terms of the correlation length's critical exponent ν and that considerably extends the result obtained by Campos Venuti and Zanardi.⁶ Perhaps even more importantly, our scaling analysis does not rely on novel concepts such as “quantum adiabatic dimension” recently advocated by Gu and coworkers.^{40,41} Also, and to the best of our knowledge, our Eq. (21) is consistent with several results for the scaling behavior of χ_F close to second order QCPs presented in the literature, including those compiled in Table I of the review Ref. 3 (note that some results from the literature quoted in this table mistake ν for $1/\nu$).

Additionally, we also obtain a scaling relation for χ_E , something that allows us to address the important point of which of the two quantities, χ_F or χ_E , is better suited in detecting quantum phase transitions. This question is particularly important from the perspective opened by the QMC SSE scheme: indeed, as we discuss in detail in Sec. III, the computational cost for calculating χ_E can be orders of magnitude smaller than the one required in obtaining χ_F , something in favor of the former as a better indicator of quantum criticality, from a practical perspective. However, our scaling analysis shows (Sec. II C) that χ_E exhibits a weaker divergence (by a factor of z in the exponent) than χ_F , meaning that it might be necessary to take into account non-divergent sub-leading corrections when performing finite size scaling analysis for χ_E . Furthermore, there may even be situations where only χ_F diverges: according to the scaling theory, this happens whenever $2/(d+z) < \nu < 2/d$. As a concrete example, we mention the case of the QCPs for the CaVO system analyzed in Ref. 8, that are preferably detected as a divergence in χ_F rather than as a cusp in χ_E .

That is, the question of which among χ_F and χ_E is best tailored to detect an unknown QCP depends on its (possibly unknown) universality class and on practical matters such as the system sizes that can be reached within SSE QMC. From a practical point of view, a pos-

sible strategy consists in evaluating χ_E on system of up to intermediate sizes (where simulations are not too demanding) and search for the presence of peaks hinting at a singularity or a cusp in the thermodynamic limit. In the affirmative case, simulations for larger systems sizes may be performed in order to confirm the occurrence of singular behavior for this quantity. If this is not the case, one should measure $\chi_F(g)$ for intermediate sizes and check on whether a singularity is more apparent.

More specifically, we compare now our results for the TIM on the square lattice to those obtained, through means of exact diagonalizations, by Yu and coworkers.³² Yu *et al.* have been able to study χ_F and χ_E by considering clusters comprising up to 20 sites and have arrived to the following estimates of critical parameters: $h_c = 2.95(1)$ and $\nu \simeq 1.40$. On the other hand, by resorting on the SSE QMC method discussed in Sec. III and on the scaling relations in Sec. II C, we are able to compute χ_F for systems with up to $N = 28 \times 28$ sites and χ_E for systems with up to $N = 48 \times 48$, arriving at the estimates (from the data collapse for χ_F performed in Sec. IV C): $h_c = 3.0440(15)$ and $\nu = 0.625(3)$. Our estimate for the location of the QCP clearly compares much better with results from conventional approaches [$h_c = 3.04438(2)$ from Ref. 31] than the one found in Ref. 32. And, even more importantly, while our result for ν is in good agreement with the known result for the universality class of the classical Ising model in $d = 3$ [$\nu = 0.6301(8)$, Ref. 37], the value for ν quoted in Ref. 32 considerably deviates from it. Again, we suspect that the value for ν is incorrectly presented as the value for $1/\nu$.

The fact that the analysis employed in Ref. 32 fails to obtain critical parameters in agreement with the ones from conventional approaches highlights the importance of the two main results presented here. First, our SSE QMC allows for the computation of χ_F and χ_E for much larger systems than possible within exact diagonalizations, enormously improving the quality of finite-size scaling analysis (we remark that results for clusters comprising less than $N = 8 \times 8$ sites are not even taken into account in the data collapse performed in Sec. IV C). Second, the scaling relations derived in Sec. II C extends previous results⁶ and expresses the scaling dimensions for both χ_F and χ_E in terms of the correlation length exponent. This has the advantage that the exponents obtained for χ_F and χ_E can be directly compared to established results for a given universality class, allowing us to decide on the validity of the approach.

We also remark that the scaling relations derived here are in agreement with the ones recently derived in the field of quantum quenches.^{16–18} In this context, the fidelity (and its susceptibility) governs the probability for the system to transit to an excited state after a sudden change of the coupling constant g away from the critical point g_c . This expands the range of applicability of the concept of fidelity susceptibility beyond the fidelity approach to quantum phase transitions.³ We might therefore expect that the QMC method presented here, or an

adaptation thereof, is also applicable in this context.

Acknowledgments

We acknowledge fruitful exchanges with O. Motrunich, A. Polkovnikov, G. Roux, D. Schwandt and L. Campos Venuti. Calculations were performed using the SSE code²³ of the ALPS libraries.³⁴ We thank CALMIP for allocation of CPU time. This work is supported by the French ANR program ANR-08-JCJC-0056-01.

Appendix A: Analytical approximation of an integral

In this section, we derive useful approximate analytical expressions for Eq. (28),

$$A(m, n) = \frac{(n-1)!}{m!(n-m-2)!} \int_0^{1/2} \tau^{m+1} (1-\tau)^{n-m-2} d\tau.$$

First, we note that $A(m, n)$ can be written in a more symmetric form

$$A(m, n) = \frac{m+1}{n} f(m+1, n-m-2),$$

where

$$f(p, q) = \frac{(p+q+1)!}{p!q!} \int_0^{1/2} \tau^p (1-\tau)^q d\tau.$$

We now concentrate on finding efficient analytical approximations for $f(p, q)$, in the limit where $r = p+q+1$ is large. Ultimately, we can apply these estimates to our practical case, corresponding to $p = m+1$, $q = n-m-2$, $r = n$.

$f(p, q)$ can be alternatively written

$$f(p, q) = \frac{\int_0^{1/2} \tau^p (1-\tau)^q d\tau}{\int_0^1 \tau^p (1-\tau)^q d\tau}.$$

After the change of variable $\tau = \frac{1}{2} \left(1 - \frac{t}{\sqrt{p+q}}\right)$, we obtain

$$f(p, q) = \frac{\int_0^{\sqrt{p+q}} \left(1 - \frac{t^2}{p+q}\right)^{\frac{p+q}{2}} \left(\frac{1 + \frac{t}{\sqrt{p+q}}}{1 - \frac{t}{\sqrt{p+q}}}\right)^{\frac{q-p}{2}} dt}{\int_{-\sqrt{p+q}}^{\sqrt{p+q}} \left(1 - \frac{t^2}{p+q}\right)^{\frac{p+q}{2}} \left(\frac{1 + \frac{t}{\sqrt{p+q}}}{1 - \frac{t}{\sqrt{p+q}}}\right)^{\frac{q-p}{2}} dt}.$$

As a first approximation in the limit $r \rightarrow \infty$, keeping fixed the ratio

$$X_1(p, q) = \frac{q-p}{\sqrt{r}}, \quad (\text{A1})$$

we obtain

$$f(p, q) \approx \frac{\int_0^\infty e^{-\frac{t^2}{2} + X_1(p, q)t} dt}{\int_{-\infty}^\infty e^{-\frac{t^2}{2} + X_1(p, q)t} dt},$$

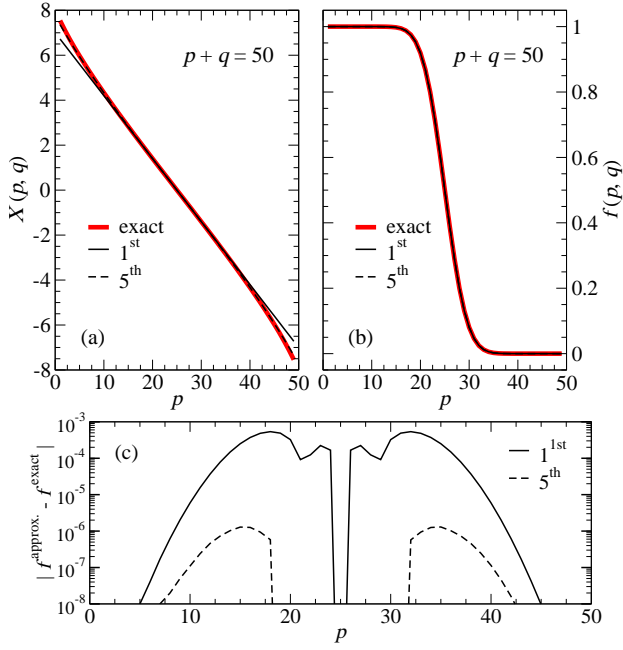


FIG. 7: (Color online) Results for (a) $X(p, q)$ and (b) $f(p, q)$ as a function of p for $p+q=50$. In both panels, the thick-full line corresponds to the “exact numerical” result, while thin-full and dashed curves are respectively first and fifth order approximations. The difference between these latter results and the exact ones for $f(p, q)$, almost indistinguishable in (b), are shown in (c). Notice that the second term in Eq. (A4) vanishes at $p=q$ [implying $f(p, q) = 1/2$ for $p=q$] and the approximations become exact at this point.

which simplifies into

$$f(p, q) \approx G[X_1(p, q)], \quad (\text{A2})$$

where

$$\begin{aligned} G(x) &= \frac{1}{\sqrt{2\pi}} \int_{-\infty}^x e^{-y^2/2} dy, \\ &= \frac{1}{2} \left[1 + \text{Erf} \left(\frac{x}{\sqrt{2}} \right) \right]. \end{aligned}$$

In order to obtain more systematic and more rigorous approximate analytic expressions for $f(p, q)$, we quite generally introduce $X(p, q)$ such that

$$f(p, q) \equiv G[X(p, q)]. \quad (\text{A3})$$

Since for $p \rightarrow +\infty$ (at fixed q), one has $f(p, q) \rightarrow 0$, we see that $X(p, q) \rightarrow -\infty$ in this limit. Moreover, the symmetry $f(p, q) = 1 - f(q, p)$ implies that $X(p, q) = -X(q, p)$.

We now look for a systematic expansion of $X(p, q)$ in powers of $(q-p)$ and expand the corresponding coefficients in (non necessarily integer) powers of $1/r$. In order

to perform this expansion, we rewrite $f(p, q)$ in the form

$$f(p, q) = \frac{1}{2} + \frac{\int_0^1 (1-t^2)^{\frac{r-1}{2}} \sinh \left[\frac{q-p}{2} \ln \left(\frac{1+t}{1-t} \right) \right] dt}{\int_0^1 (1-t^2)^{\frac{r-1}{2}} \cosh \left[\frac{q-p}{2} \ln \left(\frac{1+t}{1-t} \right) \right] dt}. \quad (\text{A4})$$

This expression is formally expanded in powers of $(q-p)$ and the corresponding coefficients are evaluated for large r . This expansion is then matched with the one obtained from a similar formal expansion of $X(p, q)$ in Eq. (A3). This calculation can be carried out with the help of MATHEMATICA, and we finally obtain the fifth order expansion in $(q-p)$ of $X(p, q)$, which generalizes the first order result of Eq. (A2). This expansion can be nicely expressed as an expansion in odd powers of $X_1(p, q)$, with coefficient having an expansion in integer powers of $1/r$:

$$\begin{aligned} X(p, q) &= a_1(r)X_1(p, q) + a_3(r)X_1^3(p, q) + \\ & a_5(r)X_1^5(p, q) + \dots, \end{aligned} \quad (\text{A5})$$

where $X_1(p, q)$ is given by Eq. (A1), and with the coefficients

$$\begin{aligned} a_1(r) &= 1 - \frac{1}{12r} - \frac{19}{160r^2} + \frac{155}{2688r^3} + \dots, \\ a_3(r) &= \frac{1}{12r} - \frac{7}{360r^2} - \frac{48929}{362880r^3} + \dots, \\ a_5(r) &= \frac{43}{1440r^2} - \frac{3253}{362880r^3} + \dots, \end{aligned}$$

which were obtained up to third order in $1/r$. As suggested by the above result, one can indeed show that the expansion of $a_{2l+1}(r)$ in powers of $1/r$ starts at order l . Hence, we find that the expansion of Eq. (A5) is valid for $|q-p| \ll r$ instead of the naive estimate $|q-p| \ll \sqrt{r}$ which could have been guessed from the quick first order calculation presented above Eq. (A2). Since one has $X(p, q) \sim \sqrt{r}$ for $|q-p| \sim r$, $f(p, q)$ is thus extremely close to 0 ($p > q$) or 1 ($p < q$) in this regime, with an error exponentially small in r . Hence, for all practical numerical purpose, it is certainly not a serious problem to have an expansion of $X(p, q)$ limited to $|q-p| \ll r$.

We now briefly illustrate the precision of the above approximate forms for $f(p, q)$ using the simplest approximation for $X(p, q)$, given in Eq. (A1), or the fifth order calculation of Eq. (A5). For the simplest first-order expression of Eq. (A2), the maximal error is less than 10^{-3} for $r > 30$, and less than 10^{-4} for $r > 275$. For the fifth order approximation, we find a maximal absolute error which is less than 10^{-5} , for $r > 25$, and less than 10^{-7} for $r > 120$.

In Fig. 7(a), we plot $X(p, q)$ as a function of p for $p+q=50$, for the first and fifth order approximations, and for the “exact numerical” $X(p, q)$ obtained after evaluating numerically the defining integral of $f(p, q)$, and inverting the relation of Eq. (A3). The plot of the three corresponding $f(p, q)$ is presented in Fig. 7(b).

The maximal error [$\sim 10^{-3}$, see Fig. 7(c)] due to the analytical approximations presented in this Appendix is

well below our Monte Carlo statistical error and for all practical purposes the first-order expression is sufficient. Indeed, only in the case of the results presented in Fig. 3, we faced the case of $r = n \lesssim 30$. Such small values of the SSE expansion order, for which the analytical ap-

proximations may become not accurate enough, are only encountered in the case of very small lattices at high temperature. In these cases, a simple pre-computation with a numerical integration of Eq. (28) for all values of (m, n) can be performed prior to simulations.

-
- ¹ P. Zanardi and N. Paunković, Phys. Rev. E **74**, 031123 (2006).
- ² L. Amico, R. Fazio, A. Osterloh, and V. Vedral, Rev. Mod. Phys. **80**, 517 (2008).
- ³ S.-J. Gu (2008), (arXiv:0811.3127).
- ⁴ P. Zanardi, P. Giorda, and M. Cozzini, Phys. Rev. Lett. **99**, 100603 (2007).
- ⁵ W.-L. You, Y.-W. Li, and S.-L. Gu, Phys. Rev. E **76**, 022101 (2007).
- ⁶ L. Campos Venuti and P. Zanardi, Phys. Rev. Lett. **99**, 095701 (2007).
- ⁷ S. Chen, L. Wang, Y. Hao, and Y. Wang, Phys. Rev. A **77**, 032111 (2008).
- ⁸ D. Schwandt, F. Alet, and S. Capponi, Phys. Rev. Lett. **103**, 170501 (2009).
- ⁹ E. Lieb, T. Schultz, and D. Mattis, Ann. Phys. B **16**, 407 (1961).
- ¹⁰ S. Katsura, Phys. Rev. **127**, 1508 (1962).
- ¹¹ P. Pfeuty, Ann. Phys. **57**, 79 (1970).
- ¹² L. Campos Venuti, M. Cozzini, P. Buonsante, F. Massel, N. Bray-Ali, and P. Zanardi, Phys. Rev. B **78**, 115410 (2008).
- ¹³ P. Zanardi, L. Campos Venuti, and P. Giorda, Phys. Rev. A **76**, 062318 (2007).
- ¹⁴ A. Uhlmann, Rep. Math. Phys. **9**, 273 (1976).
- ¹⁵ M. A. Continentino, *Quantum Scaling in Many-Body Systems* (World Scientific Publishing, Singapore, 2001).
- ¹⁶ R. Barankov (2009), (arXiv:0910.0255).
- ¹⁷ C. De Grandi, V. Gritsev, and A. Polkovnikov, Phys. Rev. B **81**, 012303 (2010).
- ¹⁸ C. De Grandi, V. Gritsev, and A. Polkovnikov (2009), (arXiv:0910.0876).
- ¹⁹ A. W. Sandvik and J. Kurkijärvi, Phys. Rev. B **43**, 5950 (1991).
- ²⁰ A. W. Sandvik, Phys. Rev. B **59**, R14157 (1999).
- ²¹ O. F. Syljuåsen and A. W. Sandvik, Phys. Rev. E **66**, 046701 (2002).
- ²² In practice, the maximum expansion order n is obviously finite. However, it is adjusted during the simulations so to ensure that the method is *exact*, in the stochastic sense. See Ref. 21.
- ²³ F. Alet, S. Wessel, and M. Troyer, Phys. Rev. E **71**, 036706 (2005).
- ²⁴ A. W. Sandvik, J. Phys. A: Math. Gen. **25**, 3667 (1992).
- ²⁵ S. Sachdev, *Quantum Phase Transitions* (Cambridge University Press, Cambridge, 1999).
- ²⁶ H.-X. He, C. J. Hamer, and J. Oitmaa, J. Phys. A: Math. Gen. **23**, 1775 (1990).
- ²⁷ J. Oitmaa, C. J. Hamer, and Z. Weihong, J. Phys. A: Math. Gen. **24**, 2863 (1991).
- ²⁸ M. S. L. du Croo de Jongh and J. M. J. van Leeuwen, Phys. Rev. B **57**, 8494 (1998).
- ²⁹ R. Rieger and N. Kawashima, Eur. Phys. J. B **9**, 233 (1999).
- ³⁰ C. J. Hamer, J. Phys. A: Math. Gen. **33**, 6683 (2000).
- ³¹ H. W. J. Blöte and Y. Deng, Phys. Rev. E **66**, 066110 (2002).
- ³² W.-C. Yu, H.-M. Kwok, J. Cao, and S.-L. Gu, Phys. Rev. E **80**, 021108 (2009).
- ³³ Simulations in the widely adopted convention for the TIM with the field in the x direction are particularly efficient using the specific algorithm presented in A.W. Sandvik, Phys. Rev. E **68**, 056701 (2003). However, computation of the parity quantum number $P = \prod_{i=1}^N \sigma_i^x |\alpha(\tau = 0)\rangle$ is then highly non-trivial, as the σ^x are now off-diagonal operators.
- ³⁴ A. F. Albuquerque, F. Alet, P. Dayal, A. Feiguin, S. Fuchs, L. Gamper, E. Gull, S. Gürtler, A. Honecker, R. Igarashi, et al., J. Magn. Magn. Mater. **310**, 1187 (2007).
- ³⁵ The processes labelled as “switch-and-reverse” and “switch-and-continue” in Ref. 21 are always allowed in the convention for the TIM adopted here, Eq. (30). See Ref. 21 for details.
- ³⁶ In general, different bipartition choices do not lead to the same results for the generalizations to finite temperatures $\chi_F(g, \beta)$ or $ds^2(g, \beta)$. Indeed, while the “quantum” parts in Eq. (12) and Eq. (14) are identical (up to a factor of g^2) whether we consider H_0 or gH_1 as the “driving term”, this is *not* the case for the “classical” contribution Eq. (13), indicating that there is no simple relationship between $\chi_F^{H_0}(\beta)$ and $\chi_F^{gH_1}(\beta)$ at finite β . However, at low enough temperature, the classical contribution becomes negligible and we recover $\chi_F^{H_0}(\beta \rightarrow \infty) = g^2 \chi_F^{gH_1}(\beta \rightarrow \infty)$, as shown in Fig. 3.
- ³⁷ H. W. J. Blöte, E. Luijten, and J. R. Heringa, J. Phys. A: Math. Gen. **28**, 6289 (1995).
- ³⁸ P. Zanardi, M. G. A. Paris, and L. Campos Venuti, Phys. Rev. A **78**, 042105 (2008).
- ³⁹ H.-G. Evertz, Adv.Phys. **52**, 1 (2003).
- ⁴⁰ S.-J. Gu and H.-Q. Lin, Europhys. Lett. **87**, 10003 (2009).
- ⁴¹ S.-J. Gu, Phys. Rev. E **79**, 061125 (2009).